

Experiments and theory of undulatory locomotion in a simple structured medium

Trushant Majmudar*, Eric E. Keaveny*,†, Jun Zhang
and Michael J. Shelley

*Courant Institute of Mathematical Sciences, 251 Mercer Street, New York University,
New York, NY 10012, USA*

Undulatory locomotion of micro-organisms through geometrically complex, fluidic environments is ubiquitous in nature and requires the organism to negotiate both hydrodynamic effects and geometrical constraints. To understand locomotion through such media, we experimentally investigate swimming of the nematode *Caenorhabditis elegans* through fluid-filled arrays of micro-pillars and conduct numerical simulations based on a mechanical model of the worm that incorporates hydrodynamic and contact interactions with the lattice. We show that the nematode's path, speed and gait are significantly altered by the presence of the obstacles and depend strongly on lattice spacing. These changes and their dependence on lattice spacing are captured, both qualitatively and quantitatively, by our purely mechanical model. Using the model, we demonstrate that purely mechanical interactions between the swimmer and obstacles can produce complex trajectories, gait changes and velocity fluctuations, yielding some of the life-like dynamics exhibited by the real nematode. Our results show that mechanics, rather than biological sensing and behaviour, can explain some of the observed changes in the worm's locomotory dynamics.

Keywords: locomotion; biofluid dynamics; fluid–structure interactions;
complex media; *C. elegans*

1. INTRODUCTION

Undulatory locomotion, as induced by the propagation of a travelling bending wave, is a mode of self-propulsion used by many species of terrestrial and aquatic organisms [1–6]. As typified by the swimming of spermatozoa, this mode of locomotion is particularly prevalent among swimming cells and small organisms moving through fluidic environments at low Reynolds number where viscous forces dominate over inertia [7–9]. While undulatory locomotion at low Reynolds numbers has been studied extensively using computational, experimental and theoretical approaches, it is often only considered in unbounded domains, or in the presence of planar boundaries [10]. There are, however, many instances in nature where swimming organisms must make their way through a fluid embedded with obstacles that are comparable in size with the swimmers themselves. One example is nematodes moving through wet soil. Another is that of mammalian sperm that swim through cervical mucus composed of an aqueous fluid matrix containing a polymeric fibre network [11]. In bovine vaginal and cervical

fluids, these fibres have a mean diameter of $0.3\text{ }\mu\text{m}$ and the network mesh size ranges from 0.7 to $27\text{ }\mu\text{m}$. This creates a meso-structure of pores 0.1 – 0.5 times the length L of the bull sperm ($L \approx 60\text{ }\mu\text{m}$) [12] through which the bull sperm must swim. Yet another example is the male gamete of the malaria parasite *Plasmodium*, which must navigate a dense suspension of red blood cells in the digestive tract of the mosquito as it searches for its female counterpart [13,14]. In this case, the male gametes have a length $L \approx 15\text{ }\mu\text{m}$ while the red blood cells are 6 – $8\text{ }\mu\text{m}$ in diameter [15] and make up greater than 50 per cent of the volume, a percentage higher than the typical hematocrit [16]. While both the mucus and red blood cell suspension themselves are examples complex fluids that can be modelled as continuous materials, the undulating body must interact with discrete elements of the embedded microstructure. These interactions lead to local hydrodynamic and contact forces experienced by the swimmer that are not incorporated into the continuum-level models.

Although each organism (mentioned earlier) has some locomotory features unique to its particular physiology, there are many open questions regarding the general nature of the motion of an undulating body swimming through a complex, obstacle-laden environment. For example, how does an organism manage to successfully navigate around the obstacles while still

*Authors for correspondence (tsm4@nyu.edu; e.keaveny@imperial.ac.uk).

†Present address: Department of Mathematics, Imperial College London, South Kensington Campus, London SW7 2AZ, UK.

Electronic supplementary material is available at <http://dx.doi.org/10.1098/rsif.2011.0856> or via <http://rsif.royalsocietypublishing.org>.

restricted by the reversibility constraints associated with viscously dominated swimming [7]? What path will it take through this composite medium and how might it vary with obstacle size or spacing? Does the organism modify its kinematics in response to the embedded structure and if so what are these changes? To what extent are changes in kinematics owing to biological sensing, or owing to a passive response induced by geometrical constraints and hydrodynamic interactions? To answer these questions, possibly applicable to many different organisms, we not only need the kinematics of their motion, but also the hydrodynamic forces, torques and contact interactions between the organism and the obstacles.

In this study, we begin to address these questions through a comprehensive set of experiments and numerical simulations by examining the changes experienced by an undulating swimmer when moving through a fluid-filled array of obstacles arranged on a square lattice. We explore in detail the changes in swimming path, wave kinematics and locomotion speed owing to the geometrical constraints and hydrodynamic forces introduced by the obstacles. For the experiments, we employ the soil-dwelling nematode *Caenorhabditis elegans* as our model undulatory swimmer and observe its motion in lattices of micro-pillars constructed from polydimethylsiloxane (PDMS). For our simulations, we construct a mechanical worm (MW) model from a chain of elastically linked beads whose undulations are driven by a wave of torques along its length. The MW model incorporates contact interactions with the obstacles and goes beyond simple drag-based approximations [17–21] of the hydrodynamic forces. We capture the swimmer–obstacle hydrodynamic interactions by solving the Stokes equations numerically and obtain the flow field generated by the undulations and the constraints imposed by the obstacles. Another key aspect of this model is that we model the forces and torques experienced by the swimmer rather than prescribing the wave kinematics directly. This allows the MW dynamics to be modified by the interactions with the lattice.

There are several reasons for choosing *C. elegans* as our model organism. *Caenorhabditis elegans* is a small nematode, approximately 1 μm in length and 60 μm in diameter, that lives in wet soil in the wild—a geometrically complex fluid-filled environment. An adult hermaphrodite is composed of 959 cells of which 302 are neurons [22]. Owing to its simple structure and ease of use in laboratory settings, *C. elegans* is one of the most widely used model organisms in modern biology. In addition, the basic characteristics of *C. elegans* locomotion are well classified. When crawling on a gel surface, *C. elegans* undulates at a mean frequency of $f_{\text{crawl}} \approx 0.7 \pm 0.1 \text{ Hz}$ with a wavelength $\lambda_{\text{crawl}} \approx 1 \text{ mm}$ and is able to move at a velocity of $v_{\text{crawl}} \approx 0.2 \text{ mm s}^{-1}$ [21,23,24]. When swimming in buffer solution with viscosity $\eta = 0.001 \text{ Pa s}$, the nematode has a higher frequency, $f_{\text{swim}} \approx 1.5\text{--}2 \text{ Hz}$, wavelength $\lambda_{\text{swim}} \approx 1.5 \text{ mm}$, but the resulting speed can have the range $v_{\text{swim}} \approx 0.1\text{--}0.35 \text{ mm s}^{-1}$ [18–21,23,25] depending on the experimental conditions.

There have also been a number of recent studies examining *C. elegans* locomotion in more complex

environments where the worm must interact with obstacles or channel walls in the plane of locomotion [26,27]. In such environments, significant and sometimes surprising changes in the locomotory behaviour of the nematode have been observed. For example, in a wet granular medium *C. elegans* is found to have a lower undulation frequency, but rather than hindering its motion, the grains allow the nematode to move in a more efficient manner, travelling a greater distance per stroke [28,29]. Park *et al.* [25] considered the locomotion of *C. elegans* through square lattices of round, short ($h \approx 100 \mu\text{m}$) posts created on the surface of an agar gel. Similar to earlier studies [28,29], they found that obstacles assist in locomotion, enabling the nematode to achieve speeds 10 times its normal swimming speed in featureless fluids.

Although these studies have shed some light on the complex navigational traits exhibited by these nematodes, a general understanding of the mechanisms that allow the worm to change the kinematics of its motion, particularly an increase in its speed, is still lacking. While there has been some theoretical work demonstrating that hydrodynamic interactions can increase swimming speeds [30], most theoretical studies of undulatory locomotion in complex media [31–35] focus primarily on the continuum limit where the fluid microstructure is small compared with the swimming body. Our study not only provides a theoretical model that includes swimmer–obstacle interaction to describe locomotion of an undulating swimmer through structured environments, but we also show a direct comparison of these results with experimental data. By considering a simple square lattice of pillars, our experiments are similar to those of Park *et al.* [25]. However, we differ in our design. Firstly, we construct the arrays from PDMS rather than agar; *C. elegans* has a strong affinity to crawl on agar surface, whereas PDMS is not conducive to crawling. Moreover, the height of the pillars ($h = 350 \mu\text{m}$) in our experiments is much larger compared with the thickness of the worm ($d \approx 60 \mu\text{m}$), which ensures that the worm remains between the pillars and does not swim above them. We compare directly the experimental and numerical results, and use both to quantify changes in the locomotion speed and swimming dynamics as the lattice spacing and undulation frequency vary. Because the MW simulations incorporate only the mechanical interactions between the undulator and the lattice, we can accurately determine their role at every stage in the dynamics. We show that not only do the mechanical interactions play a major role in the observed changes in locomotion, particularly in allowing undulatory swimmers to reach exceptionally high speeds, but they can also yield complex, ‘life-like’ paths through the lattice environment. These paths incorporate rapid fluctuations in speed, as well as changes in gait, that are characteristic to the actual worm. By comparing experiments and simulations, we show that much of the resultant behaviour observed in the experiments can be attributed purely to mechanics rather than biological sensing. On this point, we emphasize to the reader that viewing the movies in

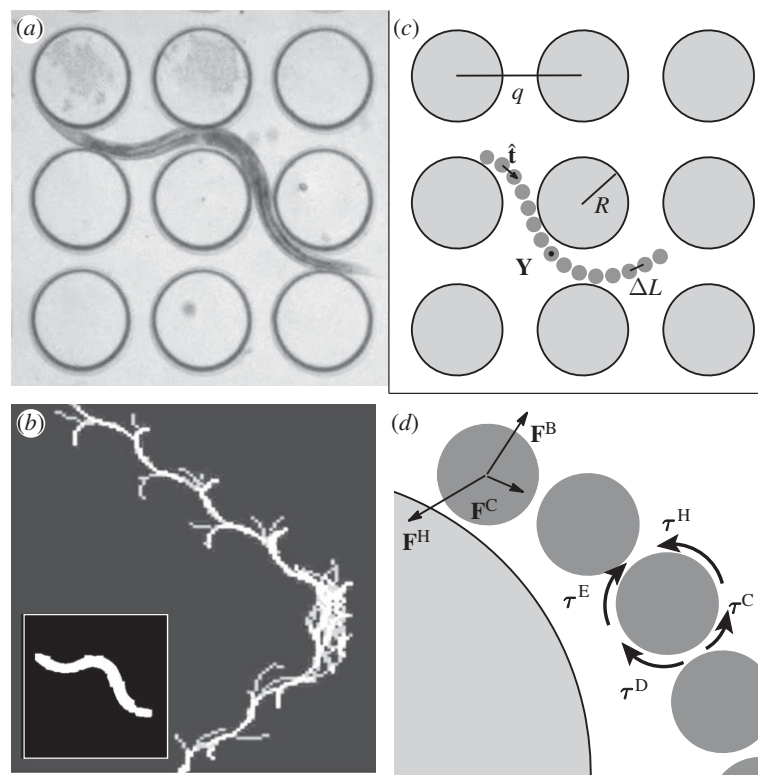


Figure 1. Experimental system and numerical model. (a) An experimental image showing *Caenorhabditis elegans* in a lattice of PDMS micro-pillars. (b) Experimental centreline of the worm in a lattice produced by superimposing multiple frames from a movie (pillars not shown). The centreline is obtained from the binarized image after background subtraction (inset). (c) The schematic of the simulation model showing the mechanical worm (MW) in a lattice of obstacles and the relevant geometrical parameters. Here, R is the radius of the obstacles, q the lattice spacing, ΔL the distance between consecutive worm segments, $\hat{\mathbf{t}}$ the tangent to the centreline and \mathbf{Y} gives the position of the centre of a segment. (d) A force and torque diagram detailing the forces and torques experienced by each segment of the MW. For the forces, \mathbf{F}^B is the repulsive contact barrier force between the segment and the obstacles, \mathbf{F}^C the constraint force owing to the inextensibility of the chain and \mathbf{F}^H the hydrodynamic force, or drag on the segment. In the case of torques, τ^E is the elastic torque that arises owing to curvature of the centreline, τ^C the constraint torque associated with centreline inextensibility, τ^D the active torque that drives the undulation and τ^H the viscous torque on the segment.

the electronic supplementary material while reading this work will be illuminating.

2. MATERIAL AND METHODS

2.1. Experiments

2.1.1. Materials

In this study, we use the wild-type *C. elegans* N2. Worms are grown on nematode growth medium plates at 20 °C, with a lawn of the bacteria OP150 as the food source. All experiments are performed with adult 3-day-old worms [22]. The lattices of micro-pillars were fabricated using standard soft photo-lithographic methods [36]. In particular, we use a photo-mask of white circles on a black background (Advanced Reproductions, MA, USA) arranged on a square lattice. We use the negative photoresist SU-8 2075 (MicroChem Inc., MA, USA) to first create a positive pattern of pillars on a silicon wafer. This SU-8 template is then used to create a negative array of PDMS holes, which is finally used to create a positive array of PDMS micro-pillars. The radii and the heights of the pillars across all lattices are the same ($R = 175 \mu\text{m}$, $H = 350 \mu\text{m}$). The centre-to-centre

distance or the lattice spacing between the pillars changes from $q = 430$ to $700 \mu\text{m}$ (figure 1), i.e. for each lattice spacing, we create a separate array and each array has a total area $A \approx 4 \text{ cm}^2$.

2.1.2. Methods

The experimental protocol consists of recording the worm locomotion in lattices via a stereo microscope (Olympus SZ 61T), under bright-field configuration (figure 1a). For this, an adult worm is transferred from the culture plate into a small Plexiglas box containing 5 ml of M9 buffer solution for washing. In this phase, the swimming worm sheds bacteria attached to its body. After 5 min, the worm is transferred to a second box containing fresh M9 solution. The free-swimming of the washed worm is recorded for 5 min at a frame rate of 10 frames per second. The worm is then transferred to a lattice of micro-pillars. The lattice has open boundaries (top and sides) and is filled with M9 buffer almost up to the height of the pillars, while ensuring that the level of fluid never reaches above the pillars. This is performed so that the nematodes always swim between the pillars and not above. In practice, this is achieved by depositing

a fixed volume of fluid using a micropipette. Each worm in a lattice is observed for 30 min. The worm-picker used to transfer the worm to the lattice stimulates the worm. As a result, during the first 3–5 min in the lattice, the worm will either remain stationary or travel within a small neighbourhood. We discard the initial 3–5 min of data from *any* subsequent analyses. Thus, we have 25 min of data for each worm in a lattice, where the worm has acclimated itself. At the end of this data collection, the worm is picked out of the lattice and placed in fresh M9 buffer and then back to a fresh agar plate with food. The process is repeated for other worms, and also for the same set of worms in other lattices. In this manner, we acquire data for an ensemble of worms of different lengths, moving in lattices with different spacing.

2.1.3. Image processing

The movies are processed via scripts written in MATLAB. The main steps involved in processing each movie consist of reading each frame, background subtraction to remove pillars from the images, thresholding the grey-scale image to create a binary image of the worm and erosion of the binary worm image to obtain the ‘skeleton’ or the centreline of the worm. Figure 1*b* shows representative images after each step. The main panel shows a representative example of the motion of the worm by superimposing multiple centrelines. The inset (figure 1*b*) shows the binary image of the worm after background subtraction, which is used to find the centreline. The centroid of the worm is also obtained to measure linear displacements and velocities, and the centreline is used to calculate the amplitude of the gait. The frequencies are obtained by frame counting. The quantities of interest that describe the mechanics of locomotion, such as the velocity and undulation frequency, are averages over multiple runs. We emphasize again that the first 3–5 min of any run are not included in the data analyses.

2.2 Numerical simulations

In our MW simulations, *C. elegans* is represented by an inextensible chain of N elastically linked spherical particles (figure 1*c*) subject to forces and torques as described here and in the electronic supplementary material. By modelling the forces and torques on the worm segments rather than prescribing their motion, the MW will change its dynamics in response to the hydrodynamic and contact interactions with nearby obstacles. The inclusion of these interactions is essential to providing an accurate characterization of the motion of the undulating body in the lattice.

In the MW, each bead, indexed by n , has radius a , is centred at \mathbf{Y}_n , and has an orientation $\hat{\mathbf{t}}_n$ (figure 1*c*). The vector $\hat{\mathbf{t}}_n$ is also used as the unit tangent to the worm’s centreline, making the ansatz that this vector varies linearly between each successive pair of beads,

$$\mathbf{t}(l) = \frac{\hat{\mathbf{t}}_{n+1} - \hat{\mathbf{t}}_n}{\Delta L} l + \hat{\mathbf{t}}_n, \quad (2.1)$$

where $l \in [0, \Delta L]$ and ΔL is the distance between the beads. The total length of the chain is, therefore, $L = N\Delta L$.

Because the Reynolds number associated with *C. elegans* swimming is small, $Re \approx 10^{-1}$, and the mass density of the worm is close to that of the surrounding fluid, we ignore the forces of inertia and gravity in our simulation model. Accordingly, the forces and torques on each bead sum to zero

$$\mathbf{F}_n^C + \mathbf{F}_n^H + \mathbf{F}_n^B = 0 \quad (2.2)$$

and

$$\boldsymbol{\tau}_n^E + \boldsymbol{\tau}_n^C + \boldsymbol{\tau}_n^D + \boldsymbol{\tau}_n^H = 0. \quad (2.3)$$

In equations (2.2) and (2.3), \mathbf{F}_n^C and $\boldsymbol{\tau}_n^C$ are constraint forces and torques, respectively, introduced to keep ΔL fixed. The torques $\boldsymbol{\tau}_n^E$ are the elastic torques associated with the worm’s flexural rigidity and are induced by curvature of the centreline. The force \mathbf{F}_n^B is a pairwise-repulsive force between the worm and the obstacles owing to solid-body contact. \mathbf{F}_n^H and $\boldsymbol{\tau}_n^H$ are the viscous forces and torques on the beads owing to the surrounding fluid. Finally, the torques $\boldsymbol{\tau}_n^D$ drive the undulation of the chain and mimic the worm’s muscular contractions. These torques are captured using a target curvature model [37] where the worm attempts to achieve a preferred time-dependent shape with curvature

$$\kappa(s, t) = -\kappa_0(s)\sin(ks - 2\pi ft), \quad (2.4)$$

where $s \in [0, L]$, and

$$\kappa_0(s) = \begin{cases} K_0, & s \leq 0.5L \\ 2K_0(L-s)L, & s > 0.5L. \end{cases} \quad (2.5)$$

Each of these forces and torques are illustrated in figure 1*d*, and a detailed description of the methods used to calculate them is provided in the electronic supplementary material.

As shown in figure 1*c*, the obstacles are spherical particles of radius R that lie in the plane of locomotion. For each obstacle n , the force and torque balance is

$$\mathbf{F}_n^C + \mathbf{F}_n^H + \mathbf{F}_n^B = 0 \quad (2.6)$$

and

$$\boldsymbol{\tau}_n^C + \boldsymbol{\tau}_n^H = 0, \quad (2.7)$$

where \mathbf{F}_n^H , \mathbf{F}_n^B and $\boldsymbol{\tau}_n^H$ represent the same forces and torques as those in the MW model. Here, the constraint forces and torques (\mathbf{F}_n^C and $\boldsymbol{\tau}_n^C$) keep the obstacles from translating and rotating, i.e. $\mathbf{V}_n = 0$ and $\boldsymbol{\Omega}_n = 0$.

To capture the hydrodynamic interactions between the worm and the obstacles, we first solve the Stokes equations numerically to determine the fluid flow, \mathbf{u} , resulting from the forces and torques on the MW and obstacles (see the electronic supplementary material). The particle velocities, \mathbf{V}_n , and angular velocities, $\boldsymbol{\Omega}_n$, are then extracted from \mathbf{u} using the force-coupling method [38,39]. The proximity of the obstacles affects the hydrodynamic forces experienced by the worm. These effects are captured approximately by the force-coupling method, though near-field lubrication forces are neglected. On the latter, a proper characterization of the lubrication layer that takes into account the compliance and corrugation of the worm cuticle is a difficult

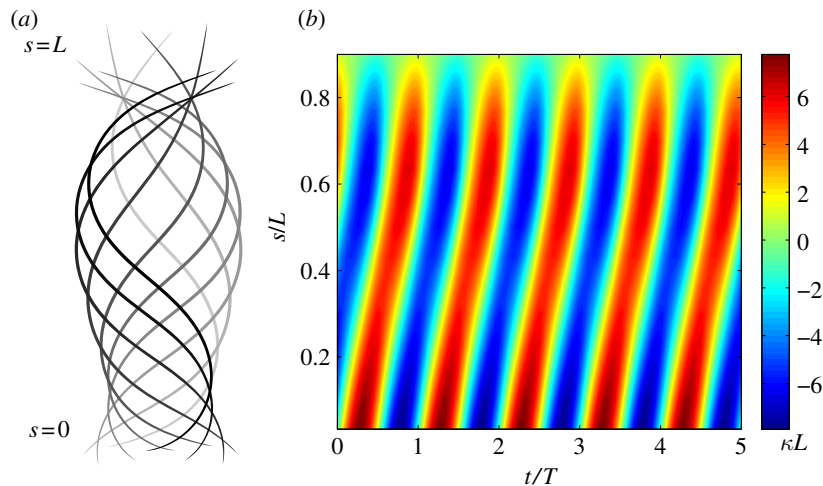


Figure 2. Wave motion and curvature of the simulated mechanical worm (MW) in the absence of obstacles. (a) The wave motion over one period for the MW model tuned to reproduce free-swimming worm-like kinematics. The parameters specifying the driving torque that yield this motion are $\mathcal{W} = 22.6$, $k = 1.5 \pi / L$, and $K_0 = 8.25 / L$. In this image, the MW is moving downward and the gray level fades as time progresses. (b) The contour image shows the propagation of the curvature waves for this free-swimming MW. These waves closely match experimentally measured values for speed and amplitude [19]. (Online version in colour.)

and open issue. Nonetheless, as we show in §3, when compared with experimental data, our simple numerical model appears to capture the basic dynamics quite well.

After computing \mathbf{V}_n and Ω_n , we then integrate the equations of motion

$$\frac{d\mathbf{Y}_n}{dt} = \mathbf{V}_n \quad (2.8)$$

and

$$\frac{d\mathbf{t}_n}{dt} = \Omega_n \times \mathbf{t}_n \quad (2.9)$$

using a second-order explicit multi-step scheme described by Karniadakis *et al.* [40].

An important parameter in the simulations is related to what is sometimes termed the Sperm number, Sp [41], but we refer to here as the Worm number, $\mathcal{W} = f\eta L^4 / K_b = Sp^4$. The Worm number provides the ratio of the viscous to elastic forces, and $b_{\mathcal{W}} = L / (\mathcal{W})^{1/4}$ is the characteristic length scale over which bending occurs when a passive elastic filament is oscillated at one end [42]. Here, however, because η , L and K_b are fixed values, \mathcal{W} functions as the dimensionless undulation frequency in the simulations.

Before examining the dynamics of the MW in the lattice, we must first tune our model in the absence of the obstacles. To match the aspect ratio, $\zeta = L/a$, of *C. elegans* ($\zeta \approx 16$), we take $N = 15$ and $\Delta L = 2.2a$. We adjust the Worm number, \mathcal{W} , as well as the wave-number, k , and amplitude, K_0 , of the preferred curvature wave (equations (2.4) and (2.5)) to replicate both the wave mechanics and the swimming speed of actual worms. We find that with $\mathcal{W} = 22.6$, $k = 1.5\pi / L$ and $K_0 = 8.25 / L$, the amplitude and speed of the resulting curvature waves closely match those measured in experiments [19]. Figure 2a shows the resulting waveform over one period for the free-swimming MW and figure 2b the propagation of curvature waves along its length. The intensity, as shown in the colourbar, corresponds to the value of the curvature scaled by the

length of the worm. For these parameters, the distance the MW travels per stroke $V/(fL) = 0.0664$ is very close to our experimental value $V/(fL) \approx 0.07$.

3. RESULTS

The motion, dynamics and speed of *C. elegans* swimming in a lattice of obstacles differ remarkably from those in a featureless viscous fluid. During free-swimming, *C. elegans* executes strokes that have the appearance of repeated concave-convex body-bends at a frequency of 1.5–2.0 Hz [18–21,23]. The resulting swimming speed can range from 0.1 to 0.35 mm s⁻¹ [19,25,28], depending on the worm's distance from the boundaries of the channel. In the micro-pillar arrays, however, the gait and speed of the worm alter owing to the geometrical constraints and modifications of the hydrodynamic forces imposed by the lattice structure. In this section, we present data from our experiments and MW simulations characterizing these effects and quantifying how the gait, the locomotory path and the speed vary as a function of the spacing between the micro-pillars. The quantitative and qualitative similarities in the experimental and MW simulation data demonstrate that mechanics and hydrodynamics, rather than biological sensing, may play a strong role in the observed phenomena.

We begin by examining the variations in the worm's trajectory through the lattice for different values of the micro-pillar spacing relative to the worm's length, q/L . (This choice stems from the fact that the number of pillars the worm comes in contact with depends on both the spacing between the pillars and its length.) Figure 3 shows experimental data for the paths traversed by the worm in lattices with $q/L = 0.37$ (a–c), $q/L = 0.47$ (d–f) and $q/L = 0.55$ (g–i). It is readily apparent that there are distinct qualitative differences in the trajectories for the different values of q/L . In the lattice with the smallest scaled spacing, where $q/L = 0.37$ (figure 3a–c and electronic supplementary

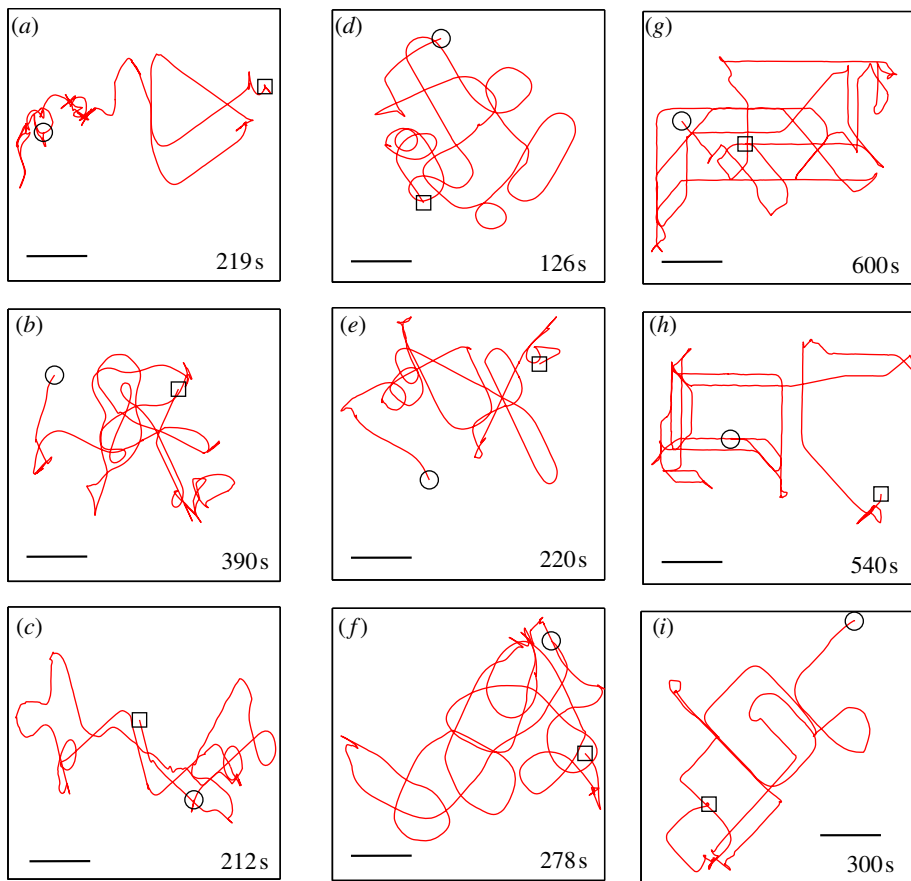


Figure 3. Experimental tracks of the worm in lattices with scaled spacings. The radius of the pillars is $175\text{ }\mu\text{m}$. The scale bar in each panel is 4 mm and each lattice is $2 \times 2\text{ cm}$ in size. The time duration for each track is also shown. In each panel, the unfilled square represents the starting point and the unfilled circle represents the end point of the path. At low values of q/L , the worm moves consistently along lattice diagonals, but becomes localized to small neighbourhoods after colliding with an obstacle. At intermediate values, along with high velocity diagonal tracks, loop-like trajectories are more common. At large values, we observe motion that is predominantly long straight-line segments, either in horizontal or vertical direction (*g,h*) or along the diagonals (*i*). (*a–c*) $q/L = 0.37$, (*d–f*) $q/L = 0.47$ and (*g–i*) $q/L = 0.55$. (Online version in colour.)

material, movie S1), the worm is in constant contact with one or more pillars and executes higher curvature, shorter wavelength undulations compared to the free-swimming gait. The typical locomotion paths consist primarily of ‘trapped’ motion in a small neighbourhood, interspersed with high velocity motion along the diagonals of the lattice. As the scaled spacing increases to $q/L = 0.47$, we observe a combination of extended high velocity diagonal tracks and looped trajectories (figure 3*d–f* and electronic supplementary material, movie S2). Here, contacts with obstacles are less frequent, and the worm can more readily weave its way through the lattice. At $q/L = 0.55$, the lattice spacing becomes comparable with the amplitude of a free-swimming worm and we find that the worm predominantly swims between rows or columns of pillars, occasionally moving along the diagonal directions (figure 3*g–i* and electronic supplementary material, movie S3). The contact between the worm and the pillars occurs very rarely and typically results in a turn and hence a change in the direction of motion.

While forward locomotion is the worm’s primary gait in the lattice, we observe instances where it exhibits other behaviours (electronic supplementary material, movie S1). For example, the worm may reverse its

direction of motion when it becomes ‘trapped’ between pillars or when it encounters a pillar head-on. We also observe the worm wrapping itself around a pillar and then unwrapping and moving in a different direction. We suspect the worm is attempting to execute an omega turn [22], but the presence of pillars constrains the extent to which it can bend its body.

Accompanying the changes in the swimming path are changes in the worm’s speed of locomotion. Figure 4*a* shows the distribution of speeds relative to the free-swimming value, V/V_0 , for the three lattices shown in figure 3. We measure the swimming speed in the absence of obstacles to be in the range $V_0 = 0.1 - 0.15\text{ mm s}^{-1}$, depending on the specific worm used in the experiment. The data are averages over multiple runs for each lattice spacing and include all types of locomotory behaviours.

The wide range of speeds the worm achieves in different lattices is immediately apparent, particularly for the cases where $q/L = 0.37$ and $q/L = 0.47$. These speeds range from values that are less than the swimming speed, $V/V_0 < 1$, when the worm is ‘trapped’ and localized to a small neighbourhood, to values that are significantly greater than its free-swimming speed. The latter is the more prevalent case for all lattice

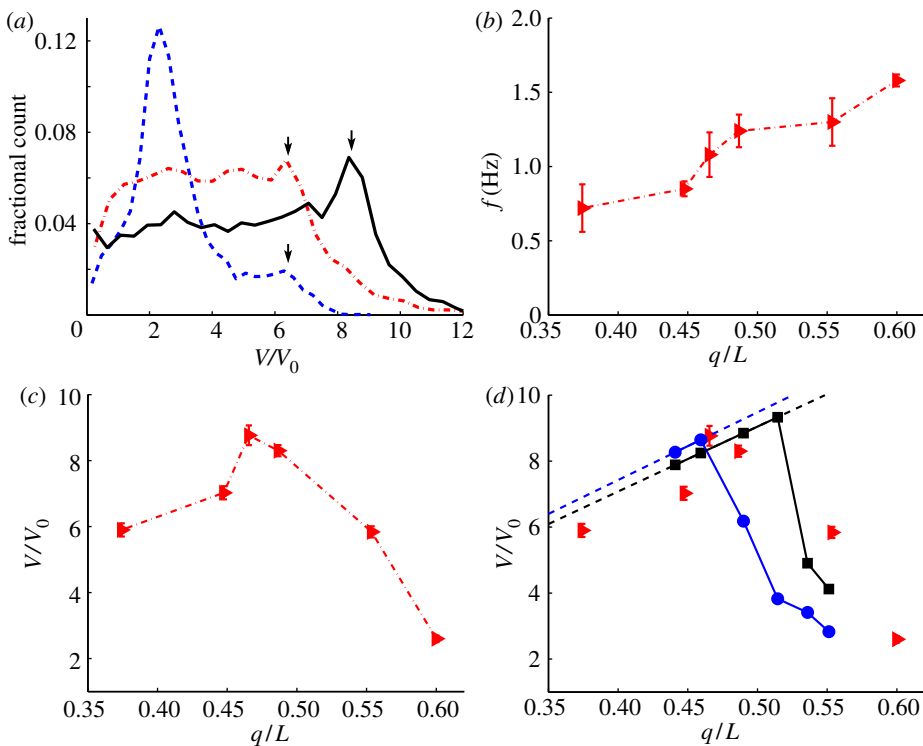


Figure 4. Velocity and frequency variations in experiments and simulations. (a) The fractional count of V/V_0 from the experiments. Each curve corresponds to one of the different values of q/L : $q/L = 0.37$ (dash-dotted line), $q/L = 0.47$ (solid line) and $q/L = 0.55$ (dashed line). The arrows point to the peaks associated with swimming along the lattice diagonals. Values below $V/V_0 = 1$ correspond to situations when the worm is ‘trapped’ and moves even slower than the free-swimming case. (b) Experimental data for the nematode’s average undulation frequency f as a function of q/L ; f monotonically increases with increasing q/L . (c) The experimentally measured values of enhanced velocity, V/V_0 , when the worm moves along the diagonal, are shown as a function of q/L . V/V_0 exhibits non-monotonic behaviour and reaches a peak value of $V/V_0 \approx 9$ when $q/L = 0.47$. (d) The solid lines with symbols show the enhanced velocity given by the mechanical worm model and are compared with the corresponding experimental values (solid triangles). The solid line with squares indicates the enhanced velocity for the simulations where $\mathcal{W} = 11.3$, whereas the solid line with the circles corresponds to those where $\mathcal{W} = 15.1$. The dashed lines indicate speeds given by $V = \sqrt{2}qf$; for both values of \mathcal{W} , the simulation data for V/V_0 follow this relation until V/V_0 reaches its peak value.

spacings. For $q/L = 0.55$, the strong peak centred around $V/V_0 \approx 2$ corresponds to the worm swimming between rows and columns of pillars. Although during this motion the worm attains speeds greater than its free-swimming value, we find that in a given lattice, the highest speeds are achieved when it moves along the lattice diagonals. The arrows in figure 4a indicate the peaks corresponding to diagonal paths. These tracks are particularly prevalent when $q/L = 0.47$, and in fact, we find that it is here that the worm achieves its highest speed $V/V_0 \approx 9$. When $q/L = 0.37$, motion along the lattice diagonals still commonly occurs, but it does so at a speed $V/V_0 \approx 6$, less than when $q/L = 0.47$. For $q/L = 0.55$, the peak corresponding to diagonal tracks is dwarfed by the one corresponding to swimming along rows. Therefore, even though the worm can achieve much higher speeds by moving along the lattice diagonals, it is more often found moving between the rows and columns of pillars.

These diagonal trajectories are of particular interest since they are where the worm achieves the highest speeds. In the subsequent analyses for motion on the diagonals, we consider only forward diagonal motion and discard any instances where the worm pauses, becomes trapped, or wraps itself around a pillar from the analyses. Before analysing how this speed

enhancement varies with lattice spacing, it is important to note that the worm’s undulation frequency also depends on the micro-pillar arrangement. Figure 4b shows the undulation frequency measured along the diagonal trajectories as a function of q/L . We see that f steadily increases from values that are close to the crawling frequency at the lowest q/L to values that approach the free-swimming frequency at high q/L . This variation in undulation frequency is evidence that the worm responds to different geometrical constraints imposed by the lattice through changes in the rate at which it flexes its musculature. Therefore, figure 4b shows the particular curve in $q/L-f$ parameter space over which *C. elegans* chooses to operate. Because the speed of locomotion will depend on both of these quantities and they can be varied *independently* in the simulations, the MW model serves as an important platform with which to explore the effects of undulation frequency and the lattice spacing independently and understand *C. elegans*’ particular choice of frequency when placed in a lattice with a given spacing.

As noted earlier and observed in Park *et al.* [25], we find that when the nematode moves along the lattice diagonals, rather than being hindered by the micro-pillars it achieves speeds that are much greater than its

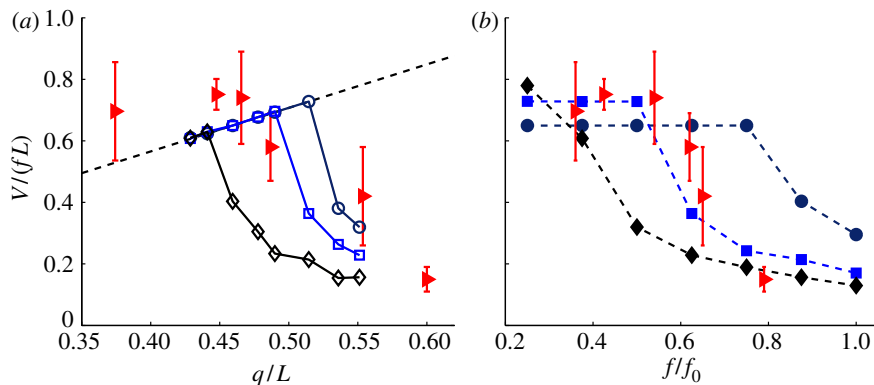


Figure 5. Variation of the scaled speed, $V/(fL)$, with q/L and f in experiments and simulations. The scaled speed provides the stroke efficiency, or the distance the worm travels in one stroke relative to its length. (a) $V/(fL)$ as a function of q/L . The solid triangles show the experimental data, whereas the solid lines with open symbols show the data from simulations for three different values of W : $W = 8.5$ (diamonds), $W = 14.1$ (squares), and $W = 17.0$ (circles). The dashed line shows the value of $V/(fL)$ when $V = \sqrt{2}qL$. (b) The plot shows $V/(fL)$ as a function of undulation frequency normalized by the free-swimming value, f_0 . The solid triangles again correspond to the experimental data, whereas the dashed lines with filled symbols show simulation data for three different values of q/L : $q/L = 0.43$ (diamonds), $q/L = 0.46$ (squares), and $q/L = 0.51$ (circles). In both (a) and (b), we see a good agreement between the experiments and simulations regarding the trends in the variation of $V/(fL)$ as a function of q/L and f/f_0 , respectively. (Online version in colour.)

free-swimming value. Figure 4c shows the experimentally measured speed relative to the free-swimming value, V/V_0 , over the diagonal tracks, as a function of the scaled lattice spacing q/L . The data shown here are from averages taken over multiple diagonal tracks of five different worms for each lattice spacing. We see that the speed depends non-monotonically on q/L where it first rises steadily to the peak value of $V \approx 9V_0$ for $q/L \approx 0.47$, then rapidly decays to $V \approx 2V_0$ for $q/L \approx 0.6$.

Now we begin to make detailed comparisons with our numerical MW model. In the simulations, we find that for the experimental obstacle size $R/L = 0.177$, the MW moves exclusively along the lattice diagonals regardless of the value of q/L . The speed at which the MW moves along this path, however, does depend on the value of q/L . In figure 4d, we compare the experimental values of V/V_0 with those determined from the MW simulations for two different values of W . The simulation data are represented by the two solid curves with squares ($W = 11.3$) and circles ($W = 15.1$), whereas the experimental data from figure 4a are superimposed as triangles. There is an excellent agreement between the experiments and the MW simulations regarding both the q/L -location of the peak velocity and the magnitude of enhanced velocity (V/V_0). Such an agreement with the MW underscores the important role of the mechanical interactions between the worm and the micro-pillars in determining the speed at which it moves through the environment. This variation in the speed of locomotion along diagonal tracks can be understood as follows. At low values of q/L , we find that the locomotion speed is governed exclusively by the geometry of the lattice and the worm's frequency of undulation. In fact, before reaching its peak value, the velocity of the MW follows closely the relation $V = \sqrt{2}qf$ (dashed lines in figure 4d), which signifies that the worm travels one row and one column per stroke. In this regime, the worm is in constant contact with the lattice, pushing off each pillar it encounters and meeting another on its back stroke.

In the frame of reference attached to the worm, the rate of arrival of the pillars is ‘in resonance’ with the frequency of undulations. The peak in enhanced velocity is achieved when q/L is such that the natural body-bends of the worm manage to partially wrap around the pillars at every half-stroke (see electronic supplementary material, movie S4). The MW simulations show that the q/L where the peak speed is realized shifts to lower values as the undulation frequency (W) increases. Beyond the peak value, the rate at which the worm encounters the obstacles no longer matches its undulation frequency, and the worm now requires multiple strokes to move a single diagonal lattice spacing. This leads to the decay in speed observed in both the experiments and MW simulations (see electronic supplementary material, movie S5). It is important to note that even at high values of q/L the speed is still twice the free-swimming value, $V/V_0 \approx 2$. Even occasional contacts with the obstacles significantly increase the speed at which the worm moves.

An important quantity that indicates the effectiveness of each of the worm's strokes is the scaled velocity, or stroke efficiency $V/(fL)$. The value of $V/(fL)$ measures the fraction of body length the worm travels in one stroke. This quantity, therefore, will vary with both the changes in the locomotion speed as well as undulation frequency. The scaled velocity as a function of q/L is shown in figure 5a. The triangles show the experimental data and the open symbols with solid lines show the data from simulations for three different values of W : $W = 8.5$ (diamonds), $W = 14.1$ (squares) and $W = 17.0$ (circles). We observe that in the experiments, up to $q/L = 0.47$ where the worm achieves its peak velocity, the scaled velocity is roughly constant with $V/fL = 0.75$ (i.e. the worm travels about 75% of its body length per stroke). Beyond this, V/fL decays with increasing lattice spacing and for the highest $q/L = 0.60$, it travels only about 10 per cent of its body length per stroke. For each of the constant W simulations, there is an initial

linear increase in the scaled velocity for low q/L . For these values of q/L , the MW moves along the lattice diagonals and its velocity follows the relation $V = \sqrt{2}qf$. The scaled velocity is therefore $V/(fL) = \sqrt{2}q/L$. This relationship between $V/(fL)$ and q/L is indicated by the dashed line in figure 5a. For each \mathcal{W} , the scaled velocity follows this relation until its peak value is reached; the peak value itself is achieved at higher q/L as \mathcal{W} increases. As in the experiments, the MW simulation data show a decrease in $V/(fL)$ over larger values of q/L .

As the worm modifies its undulation frequency in response to changes in the lattice spacing, it is important to also examine the dependence of the stroke efficiency on the undulation frequency. In figure 5b, we show the variation of the scaled velocity with respect to frequency for both the experiments and simulations. Here, the frequency is normalized by its free-swimming value, f_0 . For the experiments, the lattice spacing q/L is different for each data point, whereas each line corresponds to MW simulations with fixed q/L . We find, however, that both the experiments (triangles) and simulations (solid symbols + dashed lines) have the same trend in the data: an initial plateau region followed by a decrease in scaled velocity with increasing frequency. This plateau region corresponds to cases where the MW moves one diagonal lattice spacing in a single stroke and $V = \sqrt{2}qf$. From the MW simulations, we also see that the value f/f_0 where the plateau region ends shifts to higher values as q/L increases.

In comparing the experimental and MW simulation data, we find that not only the changes in worm dynamics, but also in quantities such as the locomotion speed are captured by our simple mechanical model. With the MW model, we may extend our results beyond the range of parameters available to the experiments as well as examine quantities that are of physical relevance, but which are not easily measurable in experiments, such as the viscous dissipation and hydrodynamic efficiency. Recall that *C. elegans* moves on the particular curve in the $q/L-f$ parameter space illustrated in figure 4b. With the MW simulation, we can explore the complete parameter space and determine how quantities such as locomotion speed vary with respect to both parameters. To do so, we compile the simulation data taken over a range of $(q/L, \mathcal{W})$ values and assemble the phase diagram shown in figure 6a. In this figure, the colour of each symbol indicates the value of $V/(qf)$ for that point in $q/L-\mathcal{W}$ parameter space. We find that enhanced locomotion along the diagonals with $V = \sqrt{2}qf$ is realized over a significant portion of $q/L-\mathcal{W}$ space as indicated in the region below the diagonal line in the diagram. As discussed earlier, this corresponds to the worm traversing one diagonal lattice spacing in one stroke. The gait of the MW in this regime is shown in figure 6c where the centreline of the worm is plotted every half undulation period. We designate this stroke as a 1–1 stroke, signifying that the worm moves 1 row and 1 column per period of undulation (see electronic supplementary material, movie S4). The diagonal line also indicates the values of \mathcal{W} where the peak speed is realized for fixed q/L . Above the line, the MW requires multiple

strokes to traverse one diagonal lattice spacing (figure 6d). The lowest $V/(qf)$ are realized when the worm requires many strokes to move one spacing (see electronic supplementary material, movie S5). These values are found at the upper right-hand corner of the diagram where both q/L and \mathcal{W} are the largest considered.

With the MW simulations, we may also examine quantities that are not readily accessible from the experiments. One important quantity that we consider here is the hydrodynamic efficiency. The hydrodynamic efficiency, $\mathcal{E} = \eta LV^2/\mathcal{D}$ [4,5], where \mathcal{D} is the average viscous dissipation over one period, provides a measure of the speed of locomotion achieved for a fixed power output per stroke. The values of \mathcal{E} are shown in figure 6b over the $q/L-\mathcal{W}$ parameter space. We find that \mathcal{E} attains its maximum along the transition boundary of the enhanced locomotion region identified as the diagonal line in figure 6a. Recall that this line also coincides with the \mathcal{W} values that yield the highest speed for fixed q/L . This indicates that as the lattice spacing increases, the undulation frequency must decrease in order for the hydrodynamic efficiency or speed to continue to realize its peak value. This is, in fact, the opposite of the trend observed in the experiments where we found that *C. elegans* undulation frequency *increases* with lattice spacing (figure 4d). This suggests that *C. elegans* is not adjusting its frequency to maximize its speed or efficiency, as what might have been suspected beforehand.

While these simulations with obstacle size $R/L = 0.177$ accurately capture the important features of diagonal, high-velocity locomotion in different lattices, we observe that the MW moves exclusively along the lattice diagonals. The experiments, not surprisingly, show that *C. elegans* exits from these diagonal tracks repeatedly and changes its direction of motion, resulting in a wide variety of paths, including loops, turns and swimming between rows or columns (figure 3). Next, we examine the motion of the MW in lattices with smaller obstacles by reducing the radius of the obstacles from $R/L = 0.177$ to 0.121. We show that this simple modification in the geometry reveals a regime in the parameter space where the MW exhibits a rich variety of dynamics similar to those observed in the experiments (see electronic supplementary material, movie S6).

The data for these MW simulations are shown in the phase diagram in figure 7. We again find two regions of parameter space; one where the MW requires a single stroke to move one diagonal lattice spacing ($V = \sqrt{2}qf$), and the other where multiple strokes are necessary ($V < \sqrt{2}qf$). The $(q/L, \mathcal{W})$ points corresponding to these two regions are the blue triangles in the lower right corner, and the cyan triangles on the upper right, respectively. For this obstacle size, we also see a third region at low values of q/L . Here, the MW is able to move out of locked diagonal tracks and exhibits the remarkable variety of complex trajectories (see electronic supplementary material, movie S6). The squares in the phase diagram indicate the $(q/L, \mathcal{W})$ where these non-diagonal trajectories are observed and the colour of the symbol designates the type of trajectory. The side panels of figure 7 show the centreline of the worm at half-period intervals for each of the different non-diagonal tracks. The light blue squares indicate parameter values where

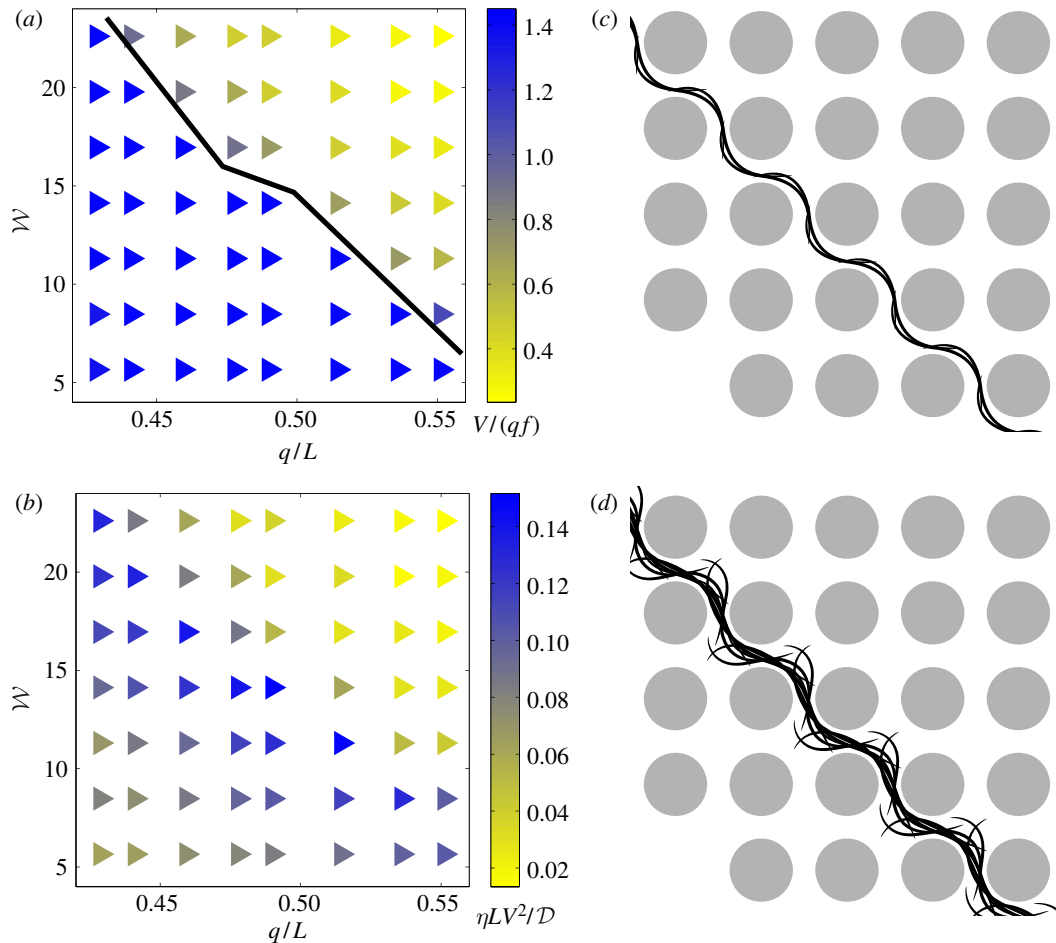


Figure 6. Simulation data over the q/L – \mathcal{W} parameter space. (a) The values of the speed normalized by the product of the lattice spacing and frequency. (b) The hydrodynamic efficiency $\mathcal{E} = \eta LV^2/\mathcal{D}$ given by the mechanical worm (MW) model is shown over the parameter space. Below the solid black line in (a), the worm requires a single stroke to move one diagonal lattice spacing and consequently $V = \sqrt{2}qf$. The gait of the MW in this regime is shown in (c) where the centreline of the worm is plotted every half undulation period. Above the line, the worm needs multiple strokes and consequently $V < \sqrt{2}qf$, as shown in (d). The hydrodynamic efficiency (b) attains its maximum values along the solid line shown in (a).

the MW executes looped trajectories. The comparable experimental paths are shown in figure 3d–f. The green squares correspond to swimming between rows of obstacles, which again was seen in the experiments (figure 3g,h). The black squares indicate cases where the MW initially moves through the lattice, but eventually undulates without translating. The pink squares indicate an asymmetric 2–1 diagonal motion where the worm moves two rows up and one column sideways. As in the 1–1 gait (figure 6c,d), the MW can take one or multiple strokes to move along the 2–1 diagonal. Both of these cases are shown in the side panel with the pink square. We also find another interesting type of motion, designated by red squares, and it is not observed in the experiments. Here, the worm weaves its way along a single column of obstacles as shown in the bottom panel of figure 7 with the red square. This mode is prevalent at very low values of both q/L and \mathcal{W} . As shown in the panel, this type of dynamics can manifest in several different ways. We find the MW can weave around one row per half-stroke (1–1 mode), or it moves in steps of two rows (2–2 mode), or it can alternate between one and two row steps (2–1 mode). All the three cases are illustrated in the bottom panel of figure 7.

The rich variety of gaits demonstrated by the MW is brought out fully when we consider the remaining data points in the parameter space, those designated by orange squares in figure 7. For these cases, the motion of the MW through the lattice is significantly more complex, resulting in *non-periodic* trajectories where the worm switches, seemingly at random, between the gaits already discussed. This gives rise to trajectories that appear ‘life-like’ but are solely the result of the contact and hydrodynamic interactions between the undulating body and the lattice of obstacles, not stochasticity or behavioural response to sensing (electronic supplementary material, movie S7).

Figure 8a shows an example of one of these trajectories and the non-periodic and ‘life-like’ nature of the path is strikingly clear (see electronic supplementary material, movie S7). The track in the main panel shows the MW in full-period intervals and the star denotes its starting point. The MW initially establishes a high velocity, 2–1 diagonal track. Box A encloses a segment of this 2–1 gait and the details of the centreline dynamics over this window are shown in the corresponding side panel. Instead of repeating this

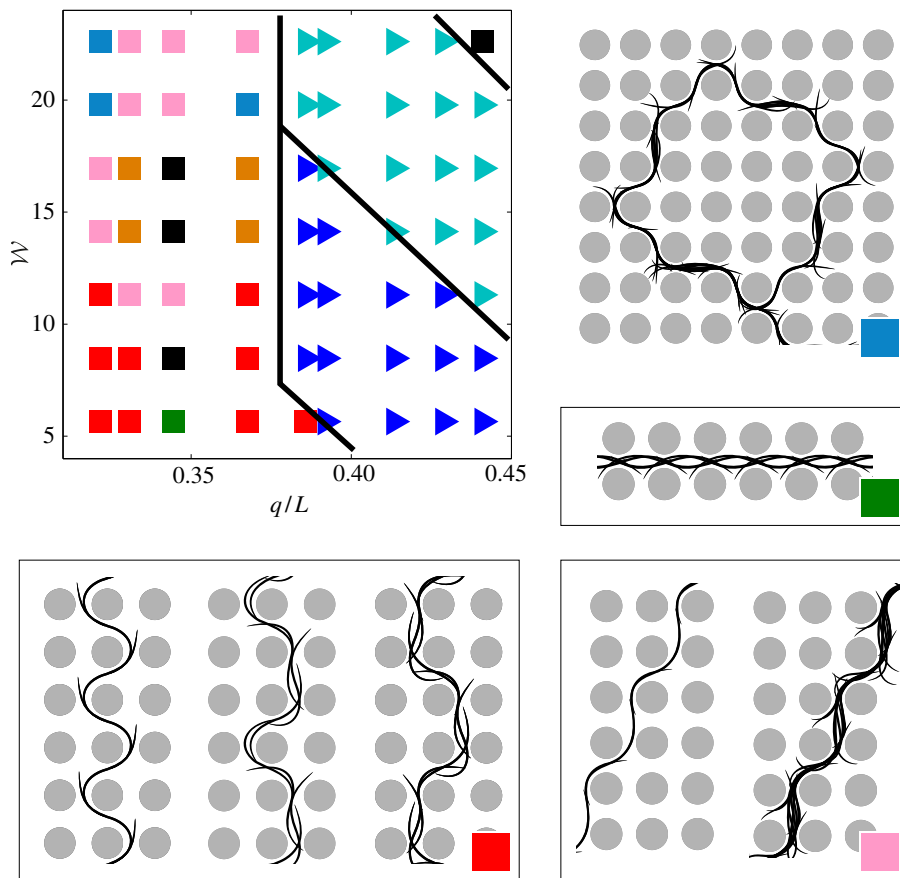


Figure 7. The phase diagram shown in the upper left-hand corner indicates the behaviour of the mechanical worm (MW) in lattices with obstacle size $R/L = 0.121$ over the $q/L-\mathcal{W}$ parameter space. In addition to finding regions where the worm moves exclusively along the lattice diagonals and requiring either one (blue triangles) or multiple (cyan triangles) strokes (figure 6), the MW also exhibits a remarkable variety of trajectories which are sensitive to the specific values of q/L and \mathcal{W} . The red squares indicate cases where the worm weaves its way around a single row or column of pillars, the pink squares correspond to an asymmetric 2–1 diagonal motion, green squares correspond to swimming between rows of obstacles and the light blue squares indicate parameter values where the MW executes closed loop trajectories. The motions of the MW corresponding to each of these cases are illustrated in the panels where the centreline of the worm is shown at half-period intervals. The black squares indicate cases where the MW initially moves through the lattice, but eventually undulates without translating. More complex non-periodic motion is also observed, indicated here by orange squares, where the worm constantly changes the way it moves through the lattice demonstrating many of the motions illustrated in the panels. This case is shown in detail in figure 8.

gait indefinitely, the MW now turns and reverses its direction of motion. This portion is enclosed in box B and shown in detail in the side panel B. The MW then transitions to swimming between two columns of obstacles, as shown within box C. The centrelines of this gait are shown in side panel C, where a number of almost in-place undulations can be observed. The MW continues to move in complex, non-periodic fashion, even beyond the time segment shown here. This behaviour is quite remarkable considering that such a realistic motion emerges from our purely mechanistic model and, moreover, accurately replicates the motion of the worm observed in the experiments. For comparison, figure 9a shows a segment of the experimental track illustrated in figure 3a. The main panel is formed by taking frames at half-period intervals from the experimental video and superimposing them over a digitally generated lattice. The boxes marked A, B and C indicate three different gaits and correspond to those exhibited by the MW: box A shows a 2–1 diagonal motion, box B shows the worm swimming

between two columns, and box C shows a turn and transition from inter-column swimming to a 2–1 diagonal motion. The side panels, marked A, B and C, show images of the centrelines of the worm plotted every half-period, for the corresponding areas in the main panel. While in a different order, we see the simulations exhibit both the gaits and transitions between them to yield an overall path that is comparable with that observed in the experiments.

Contributing to the ‘life-like’ quality of the MW’s dynamics are the abrupt changes in speed that take place as it changes gaits. Figure 8b shows the scaled velocity V/fL of the MW, as a function of time scaled by the period of the undulations. The shaded areas correspond to time windows shown in A, B and C. The scaled velocity increases from $V/(fL) \approx 0.25$ to ≈ 0.7 for window A and reaches an average of $V/(fL) \approx 0.75$ for window B where the MW turns through the lattice. The velocity then drops rapidly to $V/(fL) \approx 0.1$ for window C, where the worm swims between columns. Likewise, figure 9b shows

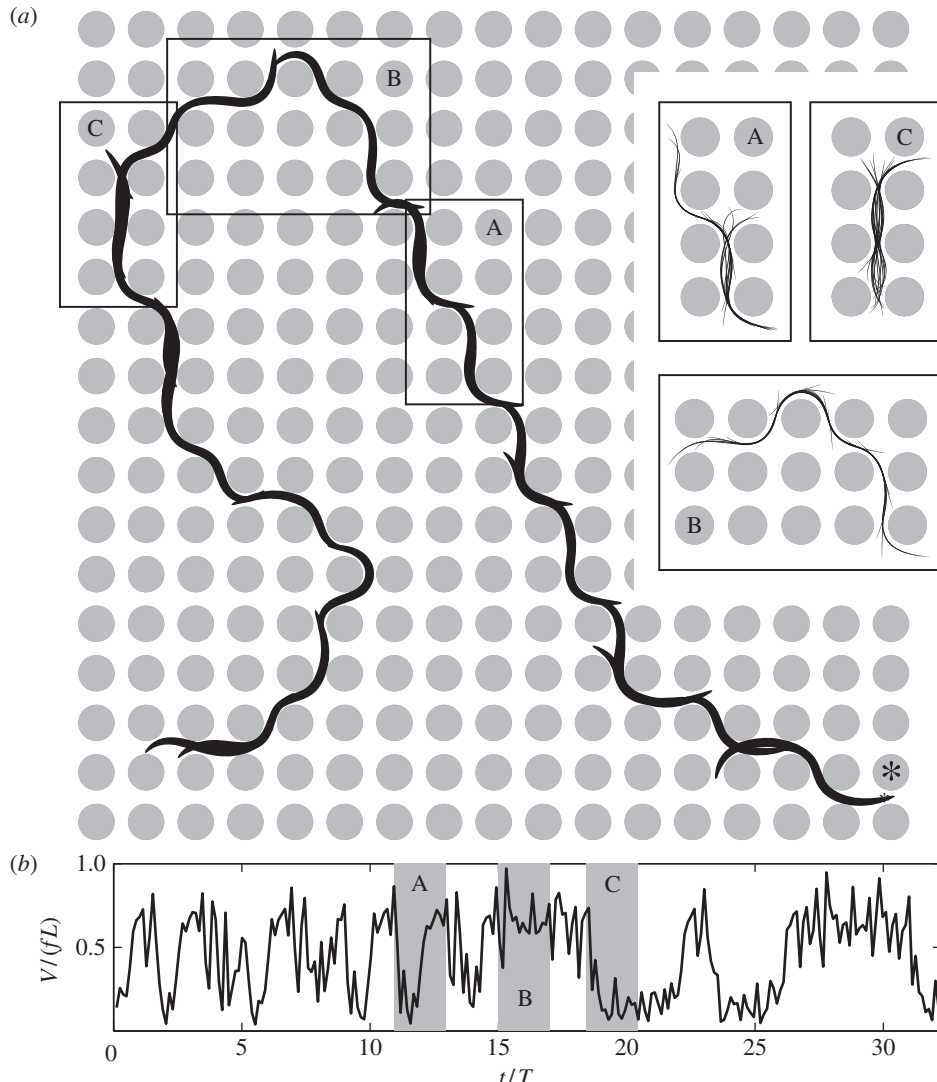


Figure 8. (a) Complex trajectory of the mechanical worm (MW) model through a lattice where $R/L = 0.121$, $q/L = 0.331$ and $\mathcal{W} = 14.1$ (see orange squares in figure 7). In the main image, the position of the centreline is plotted every undulation period and the asterisk indicates the MW's initial position. The accompanying panels show the details of the centreline motion for the indicated portions of the trajectory where the MW moves (A) along the 2–1 diagonal, (B) turning and weaving through the lattice, and (C) swimming between the rows of pillars. The inset panels show the details of the undulations in these three modes. (b) The scaled speed, $V/(fL)$, as a function of time scaled by the period of undulations. The shaded areas correspond to the time windows shown in each of the insets A, B and C, respectively.

the scaled velocity V/fL as a function of time for the experimental track. The shaded areas correspond to time windows shown in A, B and C (notice that the regions B and C in this figure are reversed with respect to figure 8). While the times spent executing the particular gaits are different, the experiments and simulations have similar average values of scaled velocity over the time period indicated for each gait. Both also exhibit characteristic fluctuations in speed that might off-hand be associated with behavioural changes, but in the case of the MW, we observe that they can occur simply from the interactions with obstacles. Further, the simulations reproduce quite well the rapid changes in speed seen in the experimental data as the worm transitions between gaits. These stop-and-go features combined with the changes in gait exhibited by the MW simulations result in overall dynamics that capture

the character of the motion of *C.elegans* in this environment.

4. DISCUSSION AND CONCLUSIONS

In this study, we have examined in detail the dynamics of locomotion of the model organism *C. elegans* through a square lattice of micro-pillars. Our experiments demonstrate that even this simple arrangement of obstacles significantly affects the nematode's wave kinematics; the speed and path of locomotion through this environment strongly depend on the lattice spacing and the degree of confinement. In particular, we found that when the worm moves along the lattice diagonals, it does so with speeds much higher than the free-swimming values and can be as much as an order of

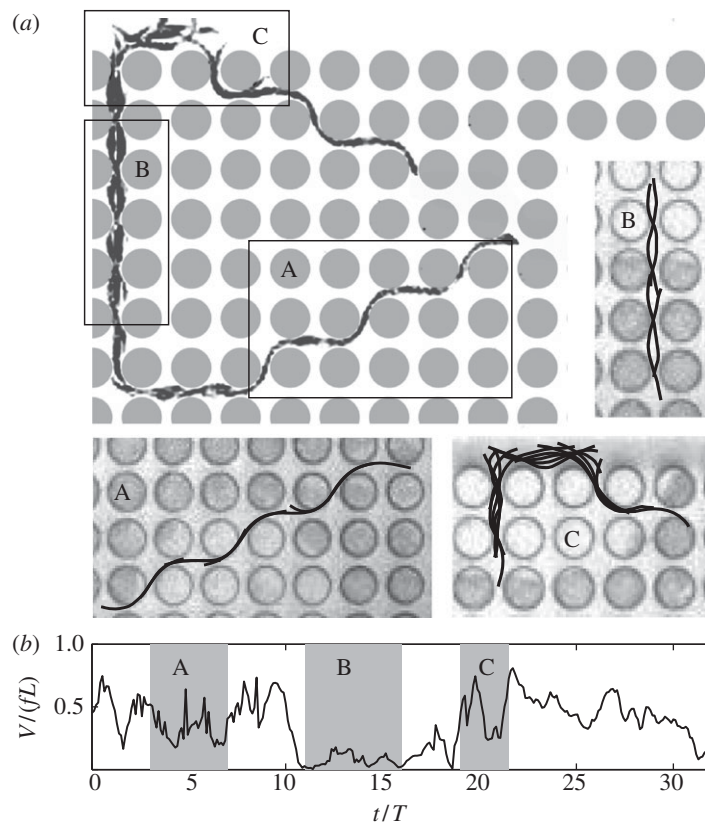


Figure 9. Complex locomotory gaits from the experiments. (a) The trajectory of the nematode through a lattice with $q/L = 0.37$ for 32 periods of undulation. As with the previous simulation results (figure 8), the worm moves (A) along the 2–1 diagonal, (B) straight between rows of pillars and (C) transitioning between these two modes. (b) The scaled speed, $V/(fL)$, as a function of time scaled by the average period of undulation. The shaded regions correspond to the time windows associated with the worm motions detailed in the panels.

magnitude greater for certain lattices. We examined these changes using the MW model that incorporates the hydrodynamic and contact interactions between the undulating worm and the obstacles. The MW model quantitatively reproduces both the high speeds observed along lattice diagonals, and its dependence on lattice spacing and undulation frequency. The obstacles function as points against which the worm can push and pull. Perhaps more surprising is that like the actual *C. elegans* worm, the MW is able to exhibit complex trajectories through the lattice where it transitions between gaits, constantly changing its direction and modifying its speed. The correspondence between the experiments and simulations reveals that some of the changes in locomotory dynamics that might, through visual inspection, be attributed to stochasticity or biophysical sensing mechanisms are primarily due to geometrical constraints and hydrodynamics.

Variations in the *C. elegans* undulation frequency have been a topic of current research, examined primarily in Newtonian fluids with different viscosities [19–21]. In these studies, the wave-form remains fixed but the frequency is found to decrease with increasing viscosity of the fluid. These experimental observations, in conjunction with the drag-based resistive force model, suggest that *C. elegans* may be using these frequency variations to maintain a constant mechanical load or power output as the viscosity of the medium

changes. Similar frequency changes have been observed in wet granular media, where the frequency decreases as the volume fraction of grains is increased [28,29]. In our experiments, a similar increase in mechanical load is to be expected as the lattice spacing decreases. We found that when placed in the lattice, *C. elegans* lowers its undulation frequency, approaching its crawling value in the lattice with the smallest spacing ($q/L = 0.37$) and steadily increasing towards the free-swimming value as the lattice spacing increases. While this modulation of frequency is exhibited by *C. elegans* in response to the changes in its surroundings, the MW simulations show that it does not correlate with maximizing hydrodynamic efficiency or locomotion speed.

As it is the mechanical interactions between *C. elegans* and the micro-pillars that lead to the increase in its speed and a modification in its path, similar changes are to be expected in other, more complex obstacle-laden environments. In random environments, for example, these mechanical interactions could allow undulatory organisms to search a greater area in a given period of time. This has indeed been observed for *C. elegans* crawling on an agar gel substrate covered with randomly distributed sand particles [43]. Speed enhancement and an increase in stroke efficiency have also been observed in *C. elegans* locomotion through wet granular media [28,29]. Here, the interactions not only produce variations in the worm's

dynamics, but also allow the worm to rearrange the surrounding grains. The effects brought about by the mechanical interactions are also not limited to *C. elegans*. Sperm cells interacting with the fibre network comprising cervical mucus may rely on these interactions to enhance their speed. In fact, the porosity of the network varies over the course of the menstrual cycle [44,45], affecting the spacing of the fibres and, consequently, changing the speed at which the sperm can swim. This mechanism of speed enhancement may also be essential to gametes of the malaria parasite, which swim through a dense suspension of red blood cells while under assault from human antibodies [13,14]. Gamete synthesis to fertilization takes under 30 min [13] and enhanced locomotion through mechanical interactions with the red blood cells could certainly contribute to the speed of this process as well. It is also interesting to note that even for terrestrial locomotion in higher organisms, such as cockroaches [46], it has been shown that mechanics plays a significant role in gait stabilization and, as in our study, speed selection.

In conclusion, we have established a combined experimental and theoretical platform, to investigate questions regarding locomotion of undulating micro-organisms in realistic, structured environments. Our approach of combining experiments and hydrodynamic simulations allows us not only to address questions regarding the locomotory behaviour of a large class of micro-organisms, but also extract information about quantities such as viscous dissipation and hydrodynamic efficiency, which are usually difficult to measure experimentally. As a result, we can accurately determine the competing effects of geometry, hydrodynamics and contact interactions on the ultimate behaviour of an undulating swimmer. In addition, our results may also have important implications for the behaviour of *C. elegans* in a realistic soil-like environment, not only in terms of its ability to navigate obstacles, but also for its overall motion in structured environments.

There are several key areas that are being investigated currently. We are experimentally investigating more complex obstacle arrangements to quantify how gradients in the obstacle locations can further affect the dynamics and speed of undulatory swimmers. We are also experimentally investigating the locomotory behaviour of a variety *C. elegans* mutants, which extend the range of geometrical and kinematic parameters. Additionally, we are conducting experiments to examine the kinematics of mechanosensory deficient *C. elegans* mutants to ascertain the role of mechanosensation on end behaviour. On the simulations front, we are currently exploring in more detail the worm's power output in the lattice by allowing the MW model to freely adjust its frequency and operate with a constant power output. Through these mutant and modified MW studies, we aim to examine the role of neural feedback, especially with regard to the frequency modulation observed in our experiments. We are also extending our MW model to explore undulatory locomotion in more complex environments by incorporating both randomness in the obstacle locations as well as obstacle compliance, bringing our MW model closer to realistic soil-like environments.

The authors acknowledge the support of the National Science Foundation under grant nos. NSF-CMMI-0700669, NSF-DMS-0652775 and NSF-DMS-0821520. The authors thank Paulo Arratia for initial help with micro-fabrication, Fabio Piano and Miyeko Mana for help with nematode growth medium plates and for the initial stock of wild-type *C. elegans*.

REFERENCES

- Gray, J. 1953 Undulatory propulsion. *Q. J. Microsc. Sci.* **94**, 551–578.
- Gray, J. 1968 *Animal locomotion*. World Naturalist Series. London, UK: Weidenfeld & Nicolson.
- Hu, D., Nirody, J., Scott, T. & Shelley, M. 2009 The mechanics of slithering locomotion. *Proc. Natl Acad. Sci. USA* **106**, 10 081–10 085. ([doi:10.1073/pnas.0812533106](https://doi.org/10.1073/pnas.0812533106))
- Lighthill, J. 1975 *Mathematical biofluidynamics*. Philadelphia, PA: SIAM.
- Childress, S. 1981 *Mechanics of swimming and flying*. Cambridge, UK: Cambridge University Press.
- Maladen, R. D., Ding, Y., Li, C. & Goldman, D. I. 2009 Undulatory swimming in sand: subsurface locomotion of the sandfish lizard. *Science* **325**, 314–318. ([doi:10.1126/science.1172490](https://doi.org/10.1126/science.1172490))
- Purcell, E. 1977 Life at low Reynolds number. *Am. J. Phys.* **45**, 3–11. ([doi:10.1119/1.10903](https://doi.org/10.1119/1.10903))
- Brennen, C. & Winet, H. 1977 Fluid mechanics of propulsion by cilia and flagella. *Annu. Rev. Fluid Mech.* **9**, 339–398. ([doi:10.1146/annurev.fl.09.010177.002011](https://doi.org/10.1146/annurev.fl.09.010177.002011))
- Fauci, L. & Dillon, R. 2006 Biofluidmechanics of reproduction. *Annu. Rev. Fluid Mech.* **38**, 371–394. ([doi:10.1146/annurev.fluid.37.061903.175725](https://doi.org/10.1146/annurev.fluid.37.061903.175725))
- Lauga, E. & Powers, T. 2009 The hydrodynamics of swimming microorganisms. *Rep. Prog. Phys.* **72**, 096601. ([doi:10.1088/0034-4885/72/9/096601](https://doi.org/10.1088/0034-4885/72/9/096601))
- Rutllant, J., Lopez-Bejar, M. & Lopez-Gatius, F. 2005 Ultrastructural and rheological properties of bovine vaginal fluid and its relation to sperm motility and fertilization: a review. *Reprod. Domest. Anim.* **40**, 79–86. ([doi:10.1111/j.1439-0531.2004.00510.x](https://doi.org/10.1111/j.1439-0531.2004.00510.x))
- Rikmenspoel, R. 1984 Movements and active moments of bull sperm flagella as a function of temperature and viscosity. *J. Exp. Biol.* **108**, 205–230.
- Paul, R., Brey, P. & Robert, V. 2002 *Plasmodium* sex determination and transmission to mosquitoes. *Trends Parasitol.* **18**, 32–38. ([doi:10.1016/S1471-4922\(01\)02122-5](https://doi.org/10.1016/S1471-4922(01)02122-5))
- Kuehn, A. & Pradel, G. 2010 The coming-out of malaria gametocytes. *J. Biomed. Biotechnol.* **2010**, 976827. ([doi:10.1155/2010/976827](https://doi.org/10.1155/2010/976827))
- Jay, A. 1975 Geometry of human erythrocyte. 1. Effect of albumin on cell geometry. *Biophys. J.* **15**, 205–222. ([doi:10.1016/S0006-3495\(75\)85812-7](https://doi.org/10.1016/S0006-3495(75)85812-7))
- Purves, W., Orians, G. & Heller, H. 2004 *Life: science of biology*, 7th edn. Sunderland, MA: Sinauer Associates.
- Niebur, E. & Erdös, P. 1991 Theory of the locomotion of nematodes: dynamics of undulatory progression on a surface. *Biophys. J.* **60**, 1132–1146. ([doi:10.1016/S0006-3495\(91\)82149-X](https://doi.org/10.1016/S0006-3495(91)82149-X))
- Berri, S., Boyle, J. H., Tassieri, M., Hope, I. A. & Cohen, N. 2009 Forward locomotion of the nematode *C. elegans* is achieved through modulation of a single gait. *HFSP J.* **3**, 186–193. ([doi:10.2976/1.3082260](https://doi.org/10.2976/1.3082260))
- Sznitman, J., Purohit, P. K., Krajacic, P., Lamitina, T. & Arratia, P. E. 2010 Material properties of *Caenorhabditis elegans* swimming at low Reynolds number. *Biophys. J.* **98**, 617–626. ([doi:10.1016/j.bpj.2009.11.010](https://doi.org/10.1016/j.bpj.2009.11.010))
- Korta, J., Clark, D. A., Gabel, C. V., Mahadevan, L. & Samuel, A. D. T. 2007 Mechanosensation and mechanical

- load modulate the locomotory gait of swimming *C. elegans*. *J. Exp. Biol.* **210**, 2383–2389. (doi:10.1242/jeb.004572)
- 21 Fang-Yen, C., Wyart, M., Xie, J., Kawai, R., Kodger, T., Chen, S., Wen, Q. & Samuel, A. D. T. 2010 Biomechanical analysis of gait adaptation in the nematode *Caenorhabditis elegans*. *Proc. Natl Acad. Sci. USA* **107**, 20 323–20 328. (doi:10.1073/pnas.1003016107)
- 22 Hall, D. H. & Altun, Z. F. 2008 *C. elegans atlas*. New York, NY: Cold Spring Harbor Laboratory Press.
- 23 Pierce-Shimomura, J. T., Chen, B. L., Mun, J. J., Ho, R., Sarkis, R. & McIntire, S. L. 2008 Genetic analysis of crawling and swimming locomotory patterns in *C. elegans*. *Proc. Natl Acad. Sci. USA* **105**, 20 982–20 987. (doi:10.1073/pnas.0810359105)
- 24 Karbowski, J., Cronin, C. J., Seah, A., Mendel, J. E., Cleary, D. & Sternberg, P. W. 2006 Conservation rules, their breakdown, and optimality in *Caenorhabditis elegans* sinusoidal locomotion. *J. Theor. Biol.* **242**, 652–669. (doi:10.1016/j.jtbi.2006.04.012)
- 25 Park, S., Hwang, H., Nam, S.-W., Martinez, F., Austin, R. H. & Ryu, W. S. 2008 Enhanced *Caenorhabditis elegans* locomotion in a structured microfluidic environment. *PLoS ONE* **3**, e2550. (doi:10.1371/journal.pone.0002550)
- 26 Lockery, S. R. et al. 2008 Artificial dirt: microfluidic substrates for nematode neurobiology and behavior. *J. Neurophysiol.* **99**, 3136–3143. (doi:10.1152/jn.91327.2007)
- 27 Qin, J. & Wheeler, A. R. 2007 Maze exploration and learning in *C. elegans*. *Lab Chip* **7**, 186–192. (doi:10.1039/b613414a)
- 28 Jung, S. 2010 *Caenorhabditis elegans* swimming in a saturated particulate system. *Phys. Fluids* **22**, 031903. (doi:10.1063/1.3359611)
- 29 Juarez, G., Lu, K., Sznitman, J. & Arratia, P. E. 2010 Motility of small nematodes in wet granular media. *Europhys. Lett.* **92**, 44002. (doi:10.1209/0295-5075/92/44002)
- 30 Leshansky, A. M. 2009 Enhanced low-Reynolds-number propulsion in heterogeneous viscous environments. *Phys. Rev. E* **80**, 051911. (doi:10.1103/PhysRevE.80.051911)
- 31 Teran, J., Faucci, L. & Shelley, M. 2010 Viscoelastic fluid response can increase the speed and efficiency of a free swimmer. *Phys. Rev. Lett.* **104**, 038101. (doi:10.1103/PhysRevLett.104.038101)
- 32 Fu, H. C., Wolgemuth, C. W. & Powers, T. R. 2008 Beating patterns of filaments in viscoelastic fluids. *Phys. Rev. E* **78**, 041913. (doi:10.1103/PhysRevE.78.041913)
- 33 Fu, H. C., Wolgemuth, C. W. & Powers, T. R. 2009 Swimming speeds of filaments in nonlinearly viscoelastic fluids. *Phys. Fluids* **21**, 033102. (doi:10.1063/1.3086320)
- 34 Fu, H. C., Shenoy, V. B. & Powers, T. R. 2010 Low-Reynolds-number swimming in gels. *Europhys. Lett.* **91**, 24002. (doi:10.1209/0295-5075/91/24002)
- 35 Lauga, E. 2007 Propulsion in a viscoelastic fluid. *Phys. Fluids* **19**, 083104. (doi:10.1063/1.2751388)
- 36 Duffy, D. C., McDonald, J. C., Schueller, O. J. A. & Whitesides, G. M. 1998 Rapid prototyping of microfluidic systems in poly(dimethylsiloxane). *Anal. Chem.* **70**, 4974–4984. (doi:10.1021/ac980656z)
- 37 Goldstein, R. E. & Langer, S. A. 1995 Nonlinear dynamics of stiff polymers. *Phys. Rev. Lett.* **75**, 1094–1097. (doi:10.1103/PhysRevLett.75.1094)
- 38 Maxey, M. & Patel, B. 2001 Localized force representation for particles sedimenting in Stokes flow. *Int. J. Multiphase Flow* **27**, 1603–1626. (doi:10.1016/S0301-9322(01)00014-3)
- 39 Lomholt, S. & Maxey, M. 2003 Force-coupling method for particulate two-phase flow: Stokes flow. *J. Comput. Phys.* **184**, 381–405. (doi:10.1016/S0021-9991(02)00021-9)
- 40 Karniadakis, G., Israeli, M. & Orszag, S. A. 1991 High-order splitting methods for the incompressible Navier–Stokes equations. *J. Comput. Phys.* **97**, 414–443. (doi:10.1016/0021-9991(91)90007-8)
- 41 Lowe, C. 2003 Dynamics of filaments: modelling the dynamics of driven microfilaments. *Phil. Trans. R. Soc. Lond. B* **358**, 1543–1550. (doi:10.1098/rstb.2003.1340)
- 42 Wiggins, C. H. & Goldstein, R. E. 1998 Flexible and propulsive dynamics of elastica at low Reynolds number. *Phys. Rev. Lett.* **80**, 3879–3882. (doi:10.1103/PhysRevLett.80.3879)
- 43 Anderson, A., Young, I., Sleeman, B., Griffiths, B. & Robertson, W. 1997 Nematode movement along a chemical gradient in a structurally heterogeneous environment. 1. Experiment. *Fundam. Appl. Nematol.* **20**, 157–163.
- 44 Morales, P., Roco, M. & Vigil, P. 1993 Human cervical mucus: relationship between biochemical characteristics and ability to allow migration of spermatozoa. *Hum. Reprod.* **8**, 78–83.
- 45 Suarez, S. & Pacey, A. 2006 Sperm transport in the female reproductive tract. *Hum. Reprod. Update* **12**, 23–37. (doi:10.1093/humupd/dmi047)
- 46 Schmitt, J., Garcia, M., Razo, R. C., Holmes, P. & Full, R. J. 2002 Dynamics and stability of legged locomotion in the horizontal plane: a test case using insects. *Biol. Cybern.* **86**, 343–353. (doi:10.1007/s00422-001-0300-3)